

Supporting Information

Molecular-enabled Lithium-locking for Stable Sorption-based Atmospheric Water Harvesting

Yating Ji^a, *Weifeng Yang*^b, *Xiaoyan Li*^a, *Jie Wang*^a, *Chengcheng Li*^a, *Jinping Zhang*^a, *Bi Xu*^a, *Charles Q. Jia*^{c,*} and *Zaisheng Cai*^{a,*}

This file includes:

1. Experimental procedure

2. Supplementary Figures

Fig. S1 Geographic distribution of world average annual relative humidity.

Fig. S2 Scatter plot of *IRI* vs $\text{sign}(\lambda_2)\rho$.

Fig. S3 Description of the color scale of the *IRI* isosurface.

Fig. S4 Photos of the Con-sponge in dry and wet states.

Fig. S5 Plot of the total energy of two systems versus time.

Fig. S6 Water leakage and lithium leakage of the two sponges after absorbing moisture.

Fig. S7 The conductivity of the two samples after 20 cycles of testing.

Fig. S8 The global annually average direct normal irradiation distribution.

Fig. S9 The hygroscopicity of Ultra-sponge under different humidity conditions.

Fig. S10 The moisture absorption kinetics data of Ultra-sponge (25 °C, 70% RH).

Fig. S11 Infrared thermal imaging photos of Con-sponge and Ultra-sponge.

Fig. S12 Evaporation rate of Ultra-sponge under different light intensities.

Fig. S13 Element distribution map of BS.

Fig. S14 Element distribution map of Con-sponge.

Fig. S15 Element distribution map of Ultra-sponge.

Fig. S16 Element content ratios of the three samples.

Fig. S17 XPS spectrums of BSP and Ultra-sponge.

Fig. S18 FTIR spectrums of BS, BSP and Ultra-sponge.

Fig. S19 Raman spectrums of PEO and PEO-0.5.

Fig. S20 Photos of crops growing after irrigation using harvested water.

Fig. S21 Comparison of tap water consumption between the control group and the experimental group.

Fig. S22 Relationship curve between shear rate and shear stress of PEO at different concentrations.

Fig. S23 Viscosity curves of PEO at different concentrations.

Fig. S24 Relationship curve between shear rate and shear stress of different samples.

Fig. S25 Viscosity curves of different samples.

Fig. S26 Hygroscopicity of samples with different lithium chloride concentrations.

3. Supplementary Tables

Table S1 Comparison of atmospheric water harvesting performance of various materials.

Table S2 Comparison of stable cyclic performance of various materials at 60% RH.

Table S3 Comparison of actual production performance of various materials.

Experimental procedure

Materials

Biochemical sponge (BS, 0.02 g cm^{-3}) was purchased from the local market. Polyethylene oxide (PEO, $M_v \sim 2,000,000$) and anhydrous lithium chloride (LiCl, 99%) were purchased from Shanghai Macklin Biochemical Technology Co., Ltd.

Preparation of Con-sponge

The BS was soaked in lithium chloride aqueous solution (0.5 M) for half an hour, during which it was squeezed continuously, and then dried at $80 \text{ }^\circ\text{C}$ for 48 hours.

Preparation of BSP

The BS was immersed in a 2 wt % PEO aqueous solution for half an hour, during which it was continuously squeezed. Following this, the sample was dried at a temperature of $80 \text{ }^\circ\text{C}$ for a period of 48 hours. The resulting sample was designated as BSP. It is noteworthy that the viscosity of the 3% PEO aqueous solution was excessively high (Fig. S22 and Fig. S23, ESI†), which hindered the uniform penetration of the mixed liquid into the biochemical sponge; therefore, a concentration of 2% was selected.

Preparation of Ultra-sponge

First, a 2 wt % PEO aqueous solution was prepared, and after the complete dissolution of PEO, varying masses of anhydrous lithium chloride were added. The concentration of lithium chloride was controlled at 0.25 M, 0.5 M, and 0.75 M respectively. These solutions were named PEO-0.25, PEO-0.5 and PEO-0.75. Subsequently, the BS was immersed within PEO-X for a duration of 30 minutes, during which it was continuously compressed to facilitate the rapid absorption of the solution by the sponge. Following this, the sample was dried at a temperature of $80 \text{ }^\circ\text{C}$ for a period of 48 hours. The names of these samples were: BSP-0.25, BSP-0.5 (Ultra-sponge) and BSP-0.75. As the concentration of lithium chloride increased, the viscosity of the solution gradually increased (Fig. S24 and Fig. S25, ESI†). This may be caused by the coordination effect and the Hofmeister effect. The best solution that matched the pore size of the biochemical sponge was PEO-0.5. We also tested the hygroscopicity of 3 samples. The results showed that the hygroscopicity of BSP-0.5 (Ultra-sponge) was significantly

higher than that of BSP-0.25 and BSP-0.75 (Fig. S26, ESI†). Therefore, the concentration of lithium chloride was selected as 0.5 M.

Moisture Sorption and Desorption tests

Moisture adsorption and desorption performance were evaluated by mass changes on an electronic balance (ME204E, Mettler, 0.1 mg). The temperature of the adsorption kinetics experiments was 25 °C and different relative humidity (30%, 50% and 70% RH) were set. The desorption experiments were performed by a solar simulator and the associated temperature changes were recorded by an infrared camera (SEEK Compact Pro. Seek Thermal, USA). The temperature/humidity detector was purchased from Jiangsu Jingchuang Electric Co., LTD. (GSP-8A).

Characterization and measurement

Scanning electron microscopy (SEM, TM1000, Hitachi Corporation of Japan) with energy dispersive spectroscopy (EDS, Quanta, FEG, 250) and Ultra-depth three-dimensional microscope (UTM, VHX-6000) were used to characterize the microscopic morphology of samples. Fourier transform infrared spectrometer (FTIR, NICOLET iS10, Thermo Fisher Scientific), X-ray diffractometer (XRD, Bruker D8 ADVANCE) and X-ray photoelectron spectroscopy (XPS, Escalab 250Xi) were applied to analyze the chemical components and surface functional groups of samples. Textile strength tester (YG026Q, Ningbo textile instrument factory, China) was used to analyze the strength change of the sponge before and after preparation.

Statistical Analysis

Error bars represent standard deviation (SD).

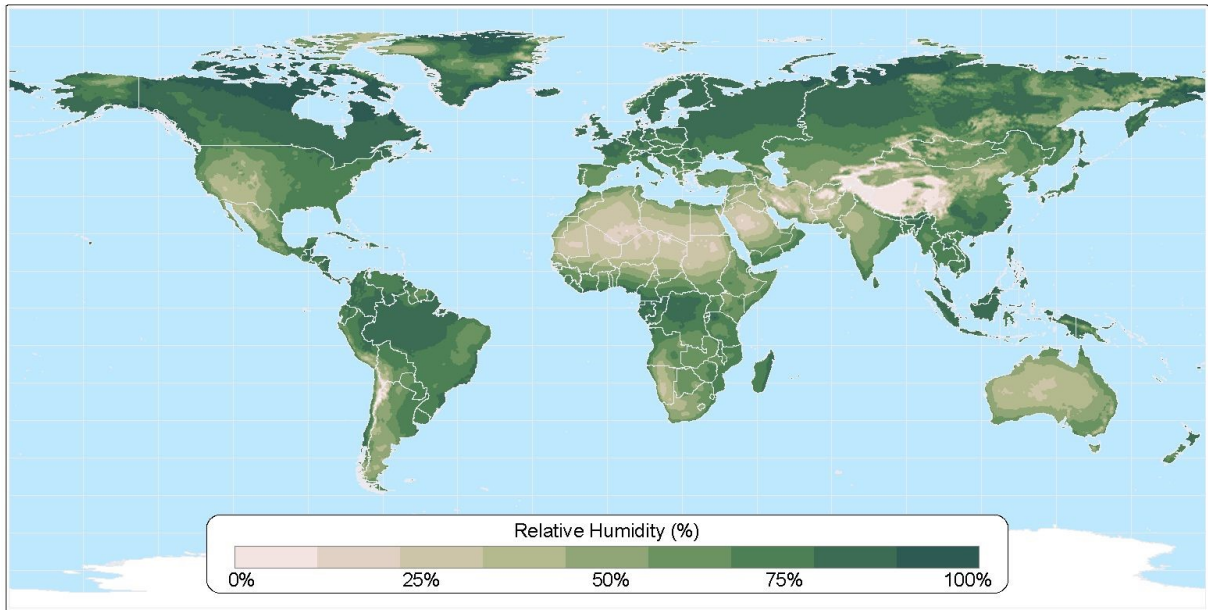


Fig. S1 Geographic distribution of world average annual relative humidity. Data sourced from Center for Sustainability and the Global Environment (sage.nelson.wisc.edu).

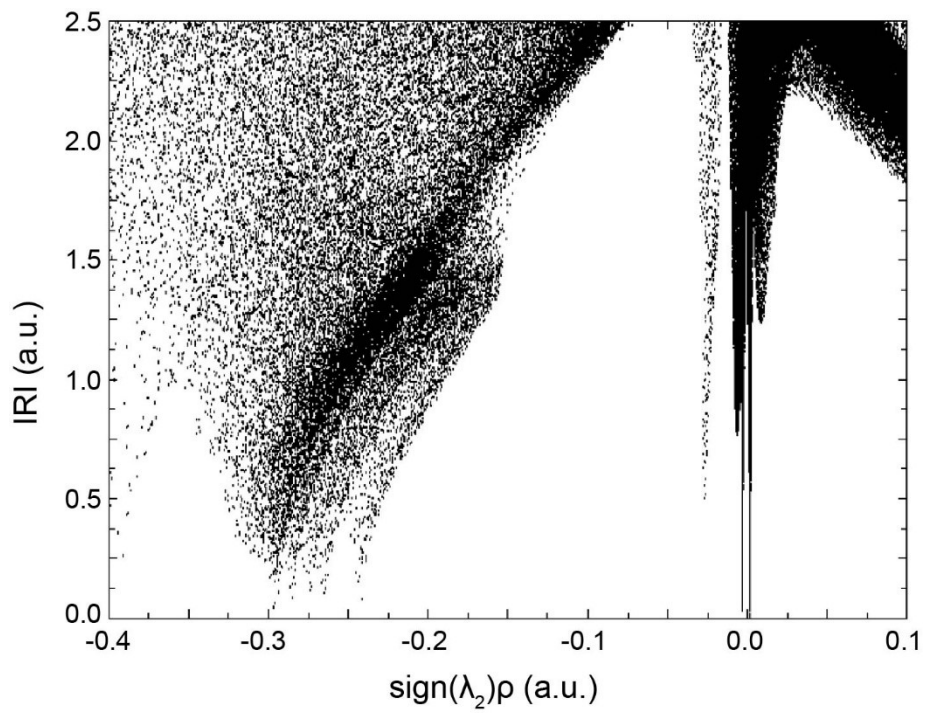


Fig. S2 Scatter plot of IRI vs $sign(\lambda_2)\rho$.

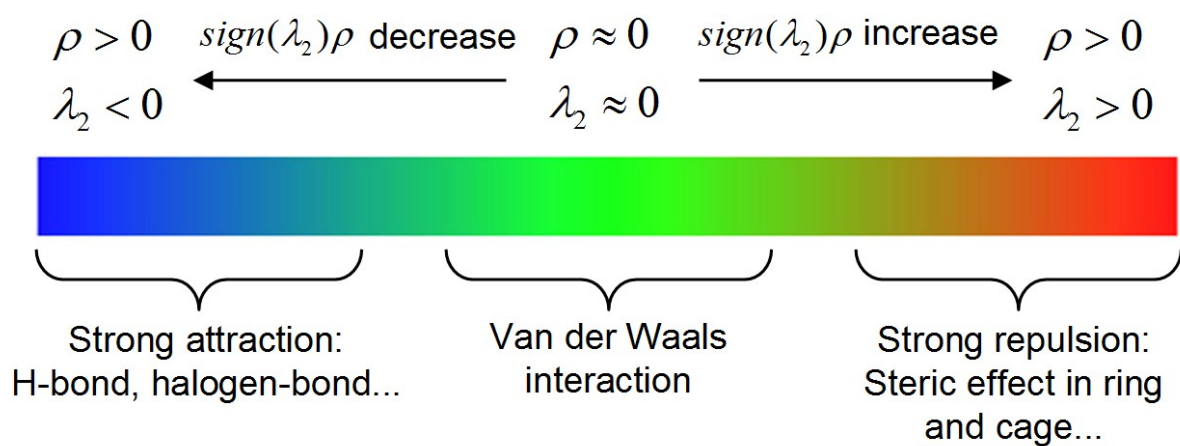


Fig. S3 Description of the color scale of the *IRI* isosurface.

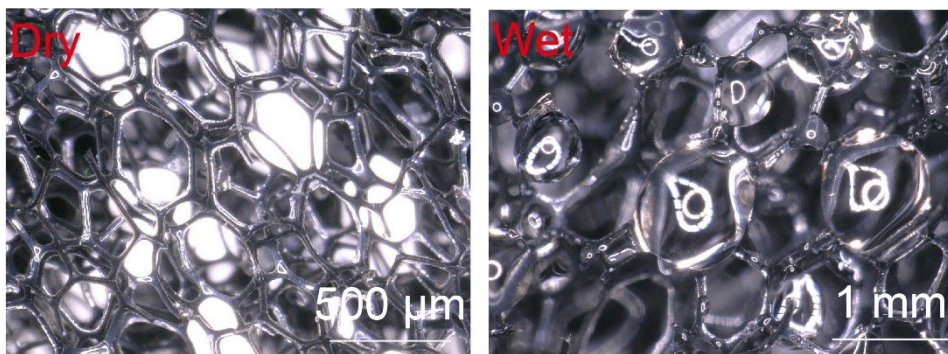


Fig. S4 Photos of the Con-sponge in dry and wet states.

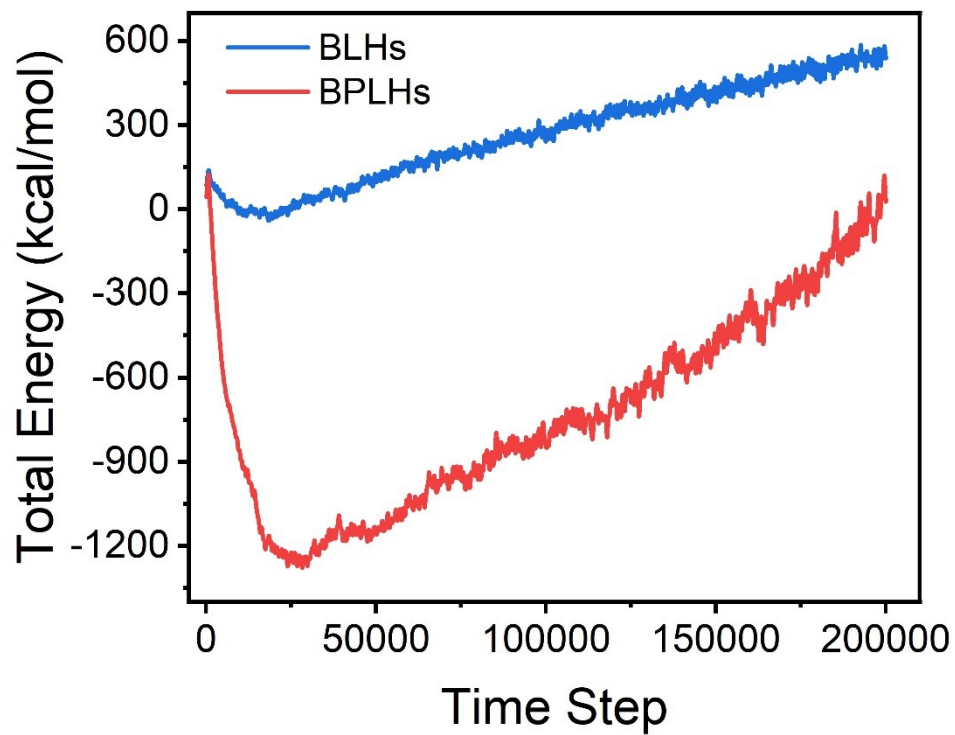


Fig. S5 Plot of the total energy of two systems versus time.

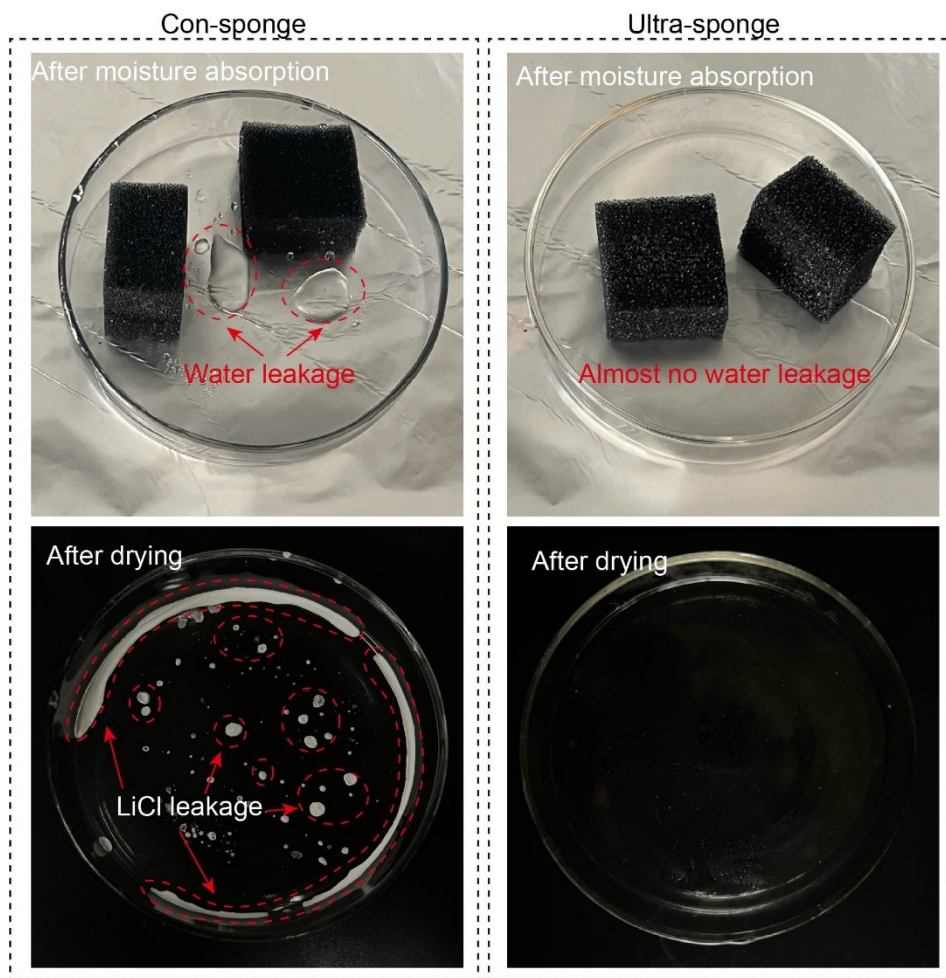


Fig. S6 Water leakage and lithium leakage of the two sponges after absorbing moisture.

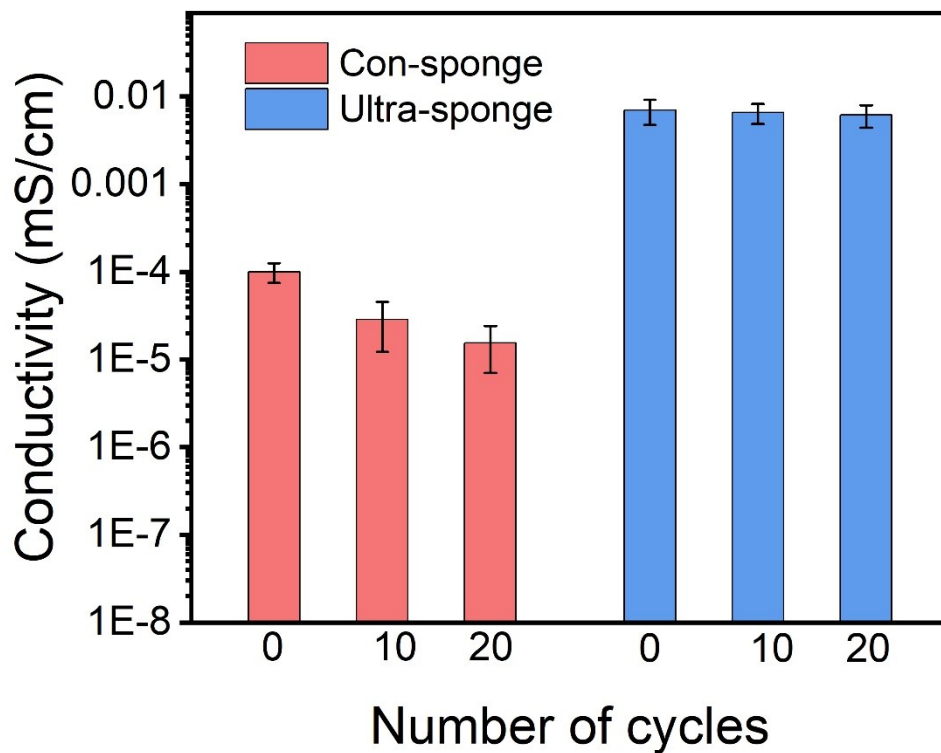


Fig. S7 The conductivity of the two samples after 20 cycles of testing.

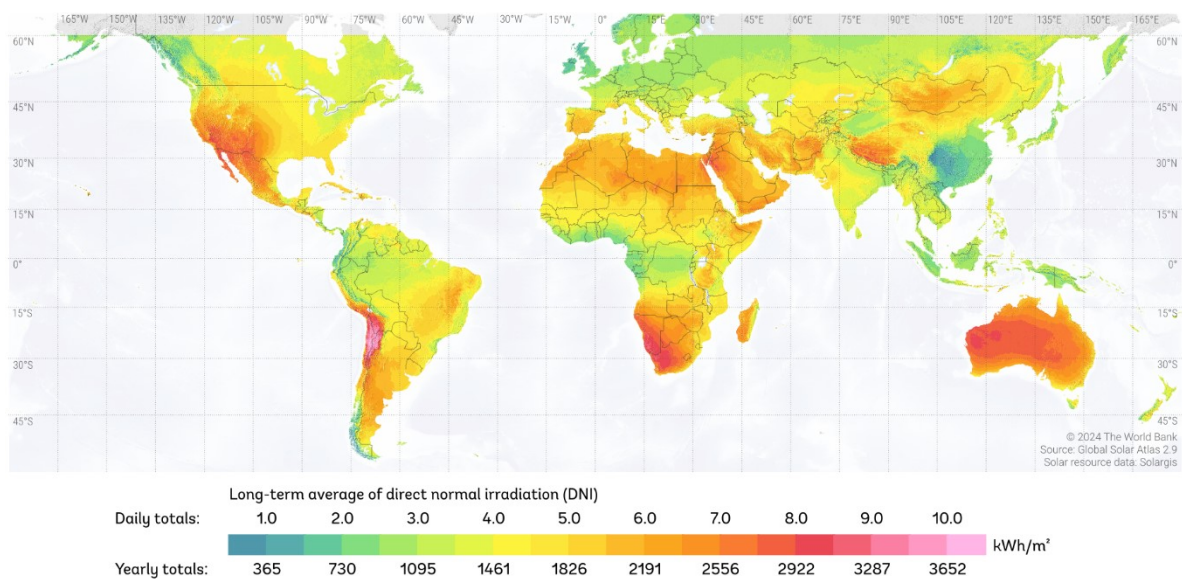


Fig. S8 The global annually average direct normal irradiation distribution. Data sourced from Global Solar Atlas (globalsolaratlas.info).

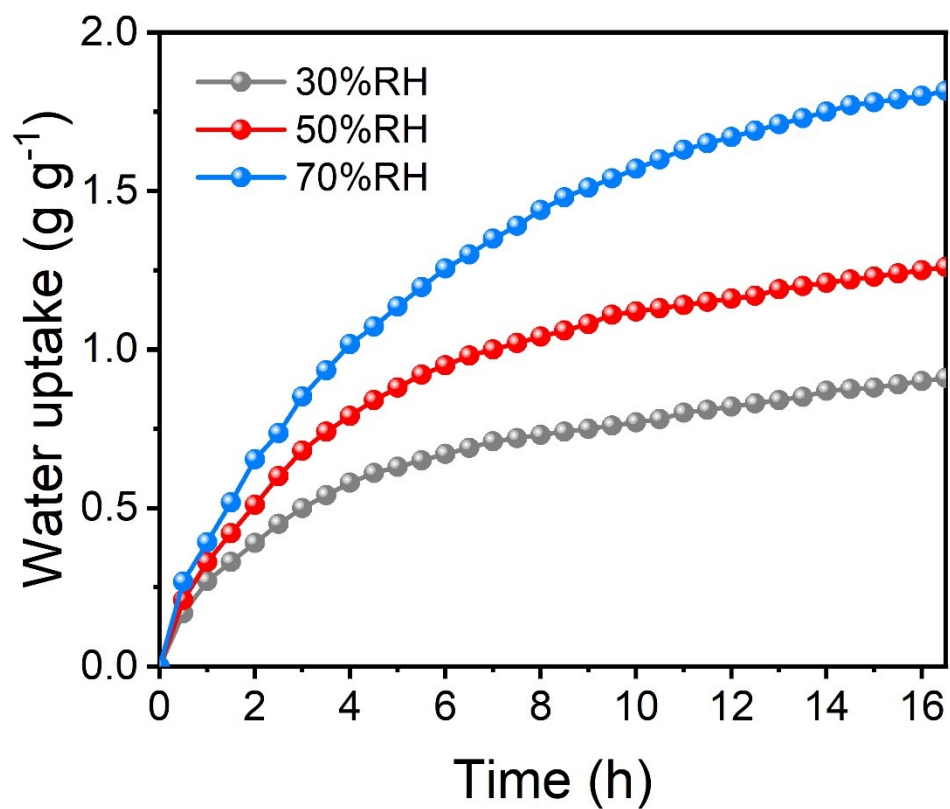


Fig. S9 The hygroscopicity of Ultra-sponge under different humidity conditions.

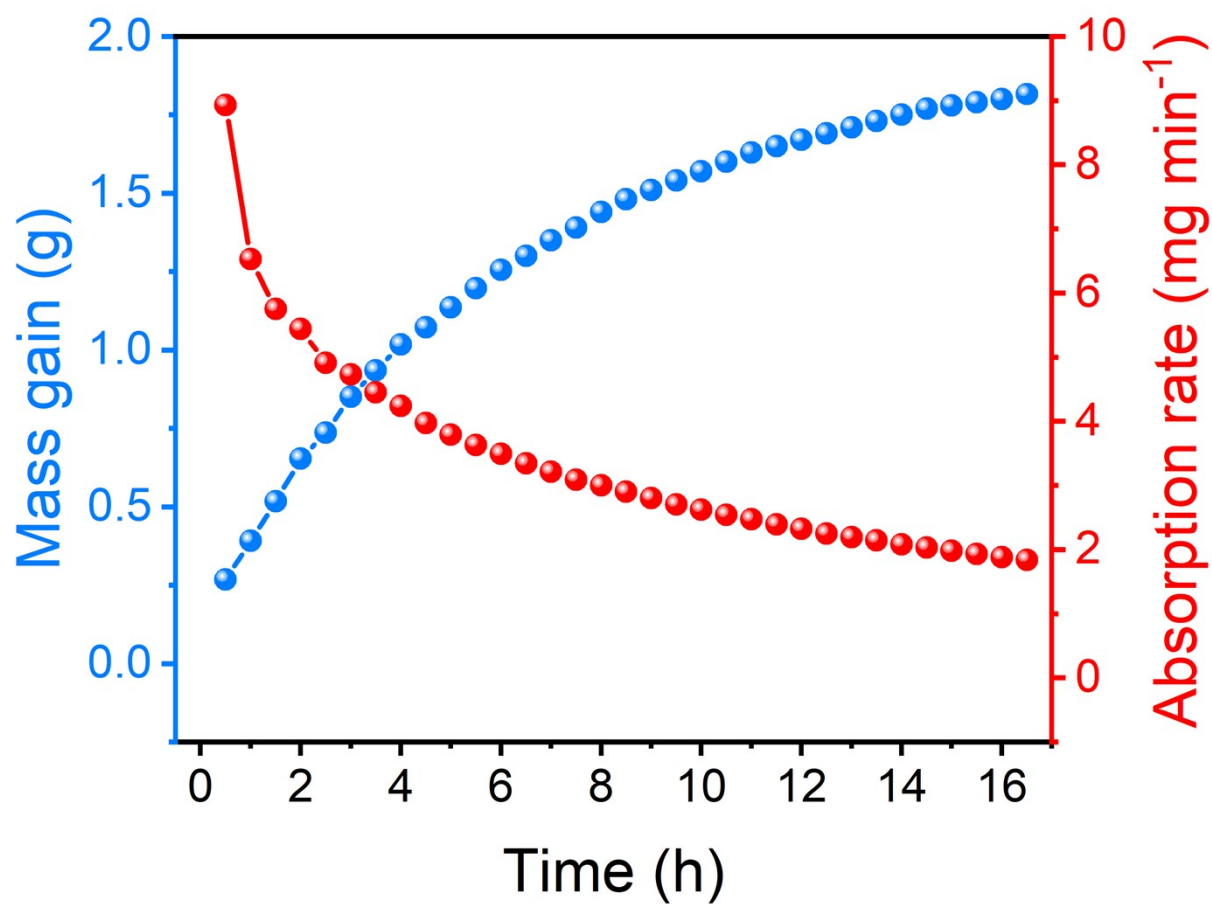


Fig. S10 The moisture absorption kinetics data of Ultra-sponge (25 °C, 70% RH).

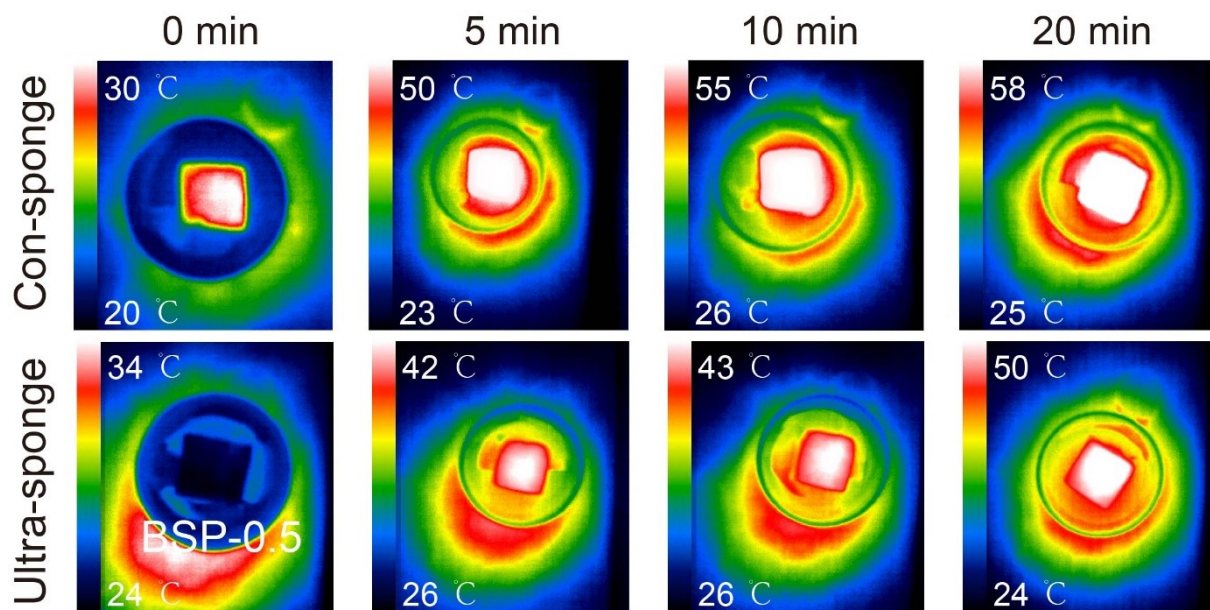


Fig. S11 Infrared thermal imaging photos of Con-sponge and Ultra-sponge.

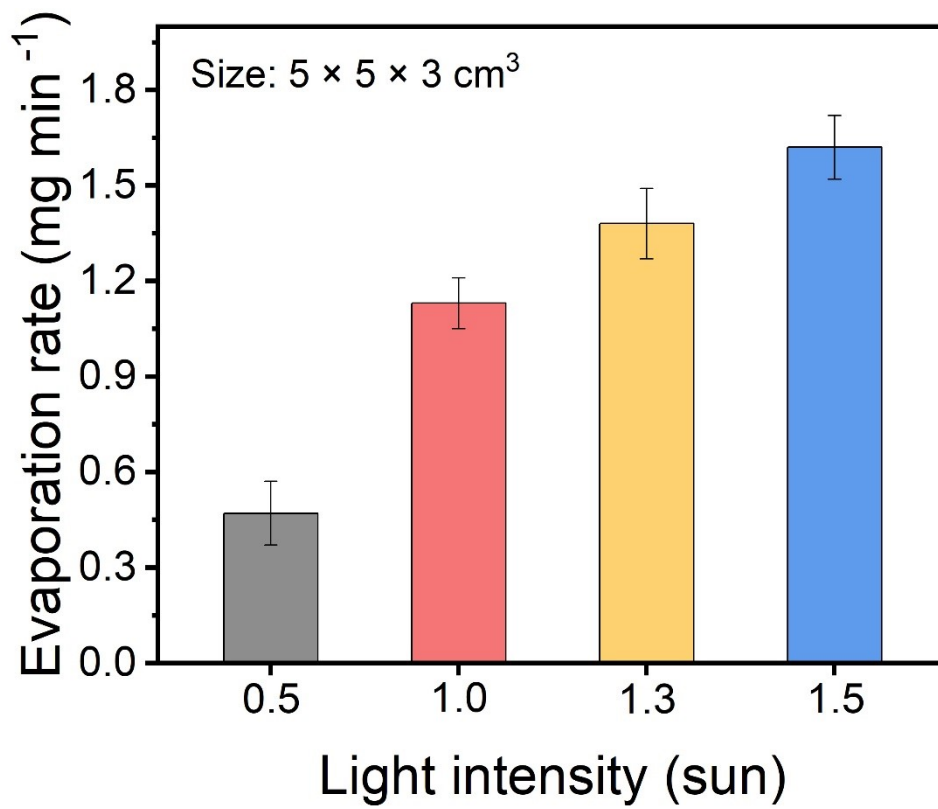


Fig. S12 Evaporation rate of Ultra-sponge under different light intensities.

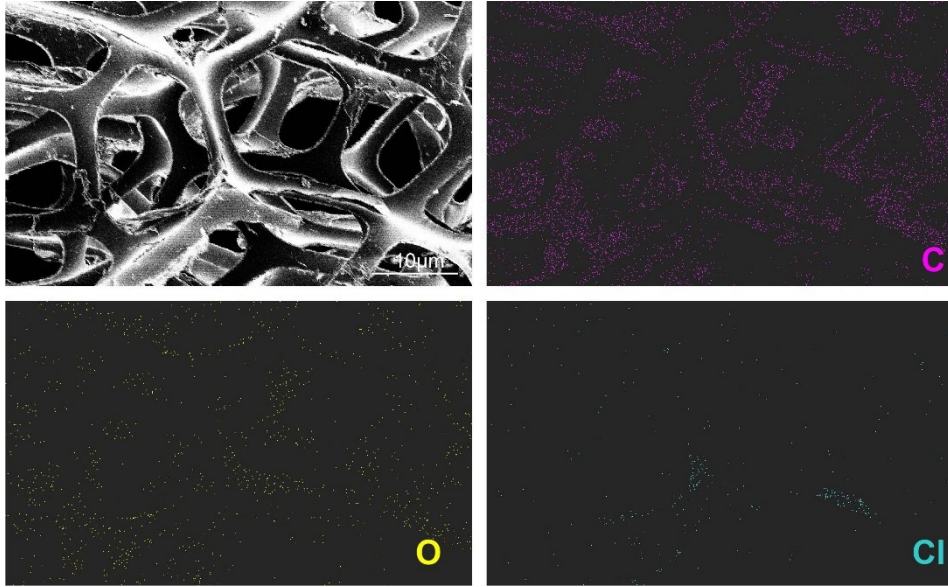


Fig. S13 Element distribution map of BS.

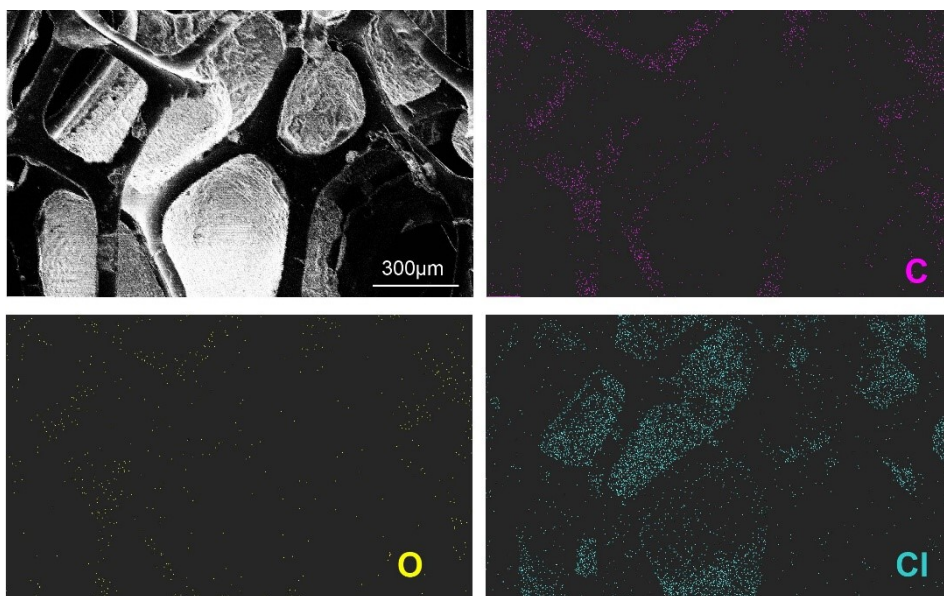


Fig. S14 Element distribution map of Con-sponge.

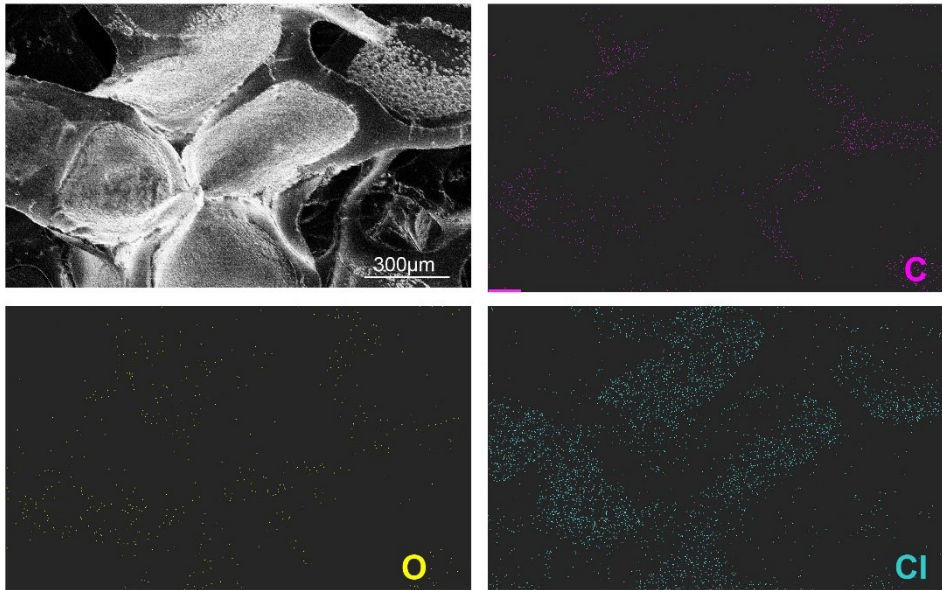


Fig. S15 Element distribution map of Ultra-sponge.

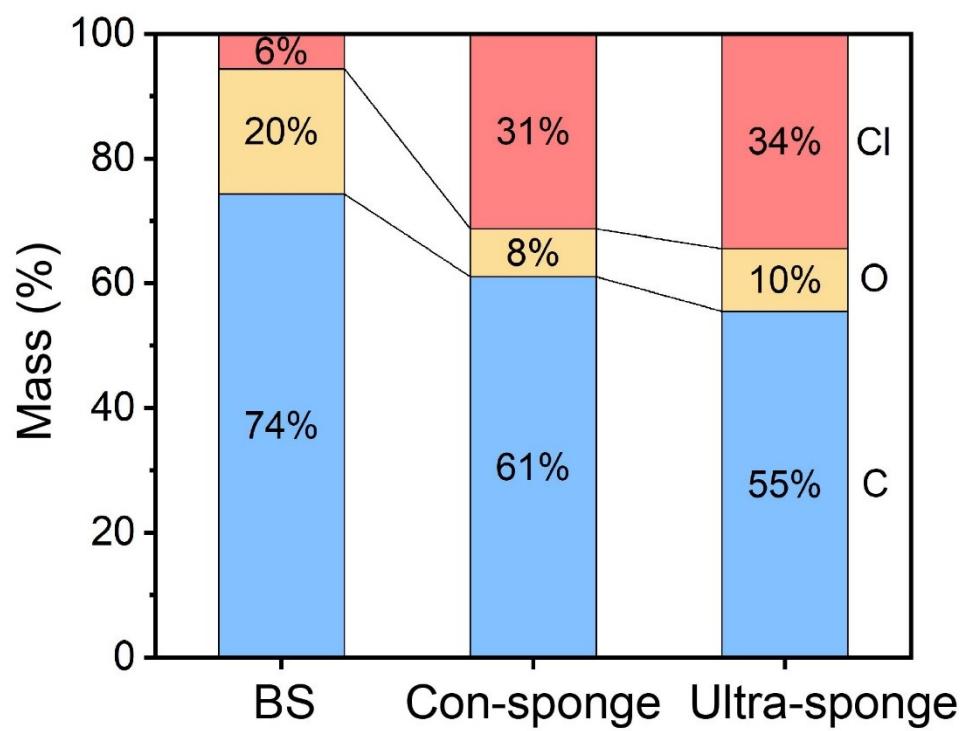


Fig. S16 Element content ratios of the three samples.

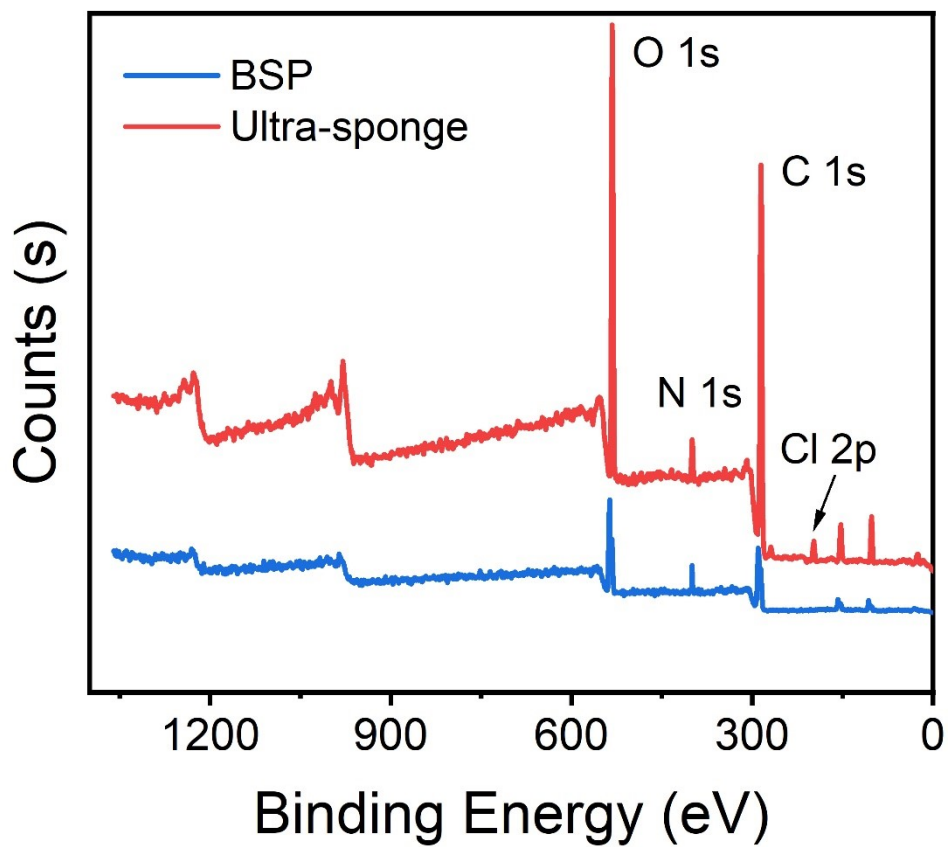


Fig. S17 XPS spectrums of BSP and Ultra-sponge.

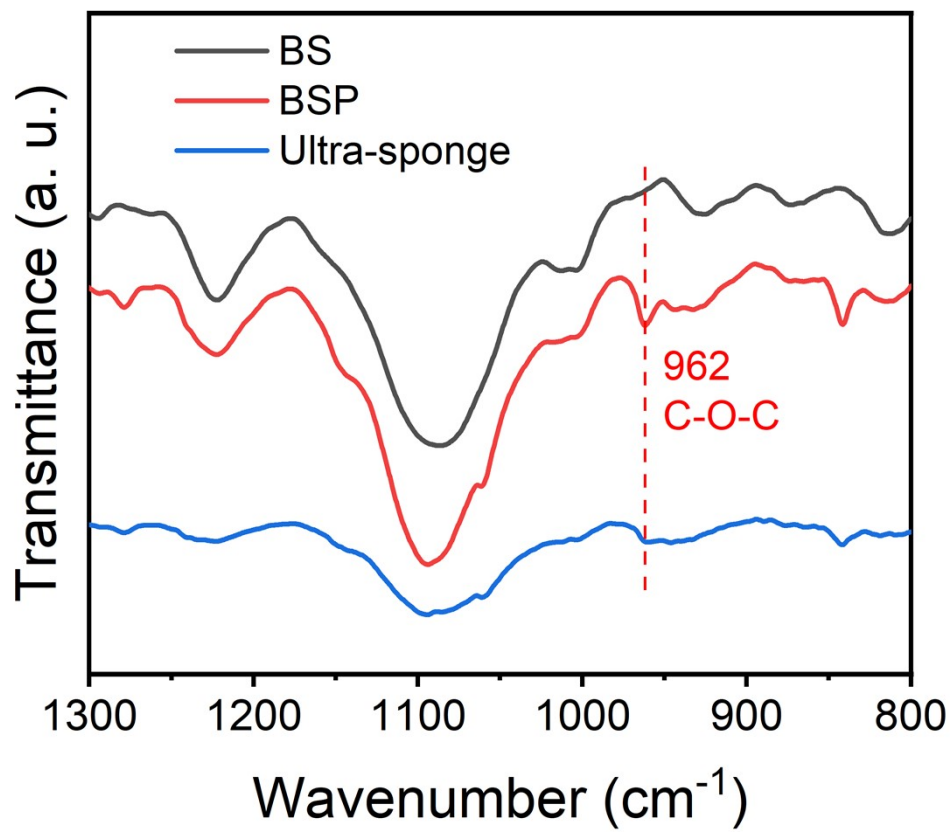


Fig. S18 FTIR spectrums of BS, BSP and Ultra-sponge.

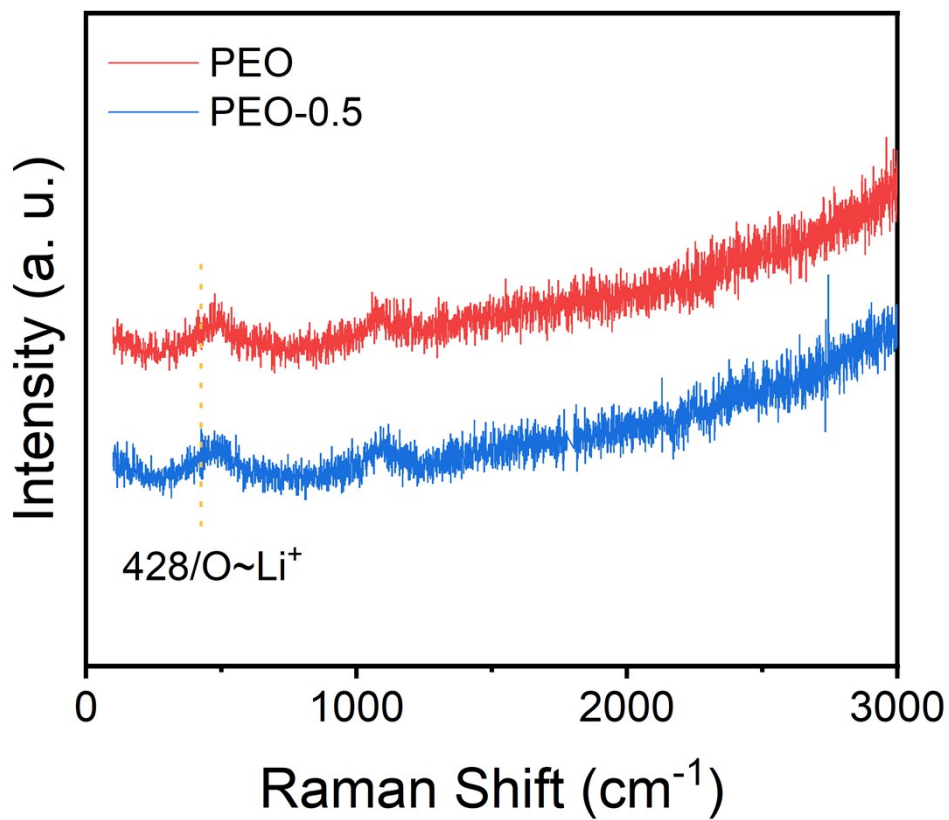


Fig. S19 Raman spectrums of PEO and PEO-0.5.

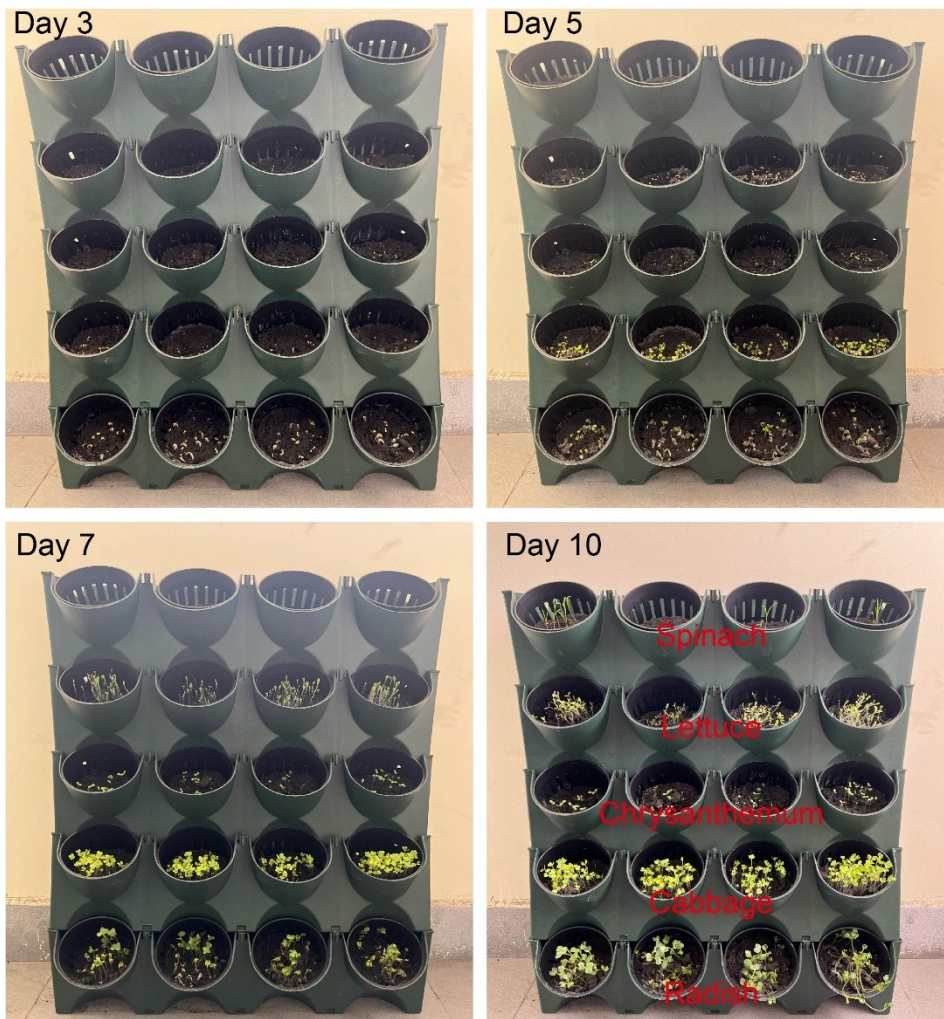


Fig. S20 Photos of crops growing after irrigation using harvested water.

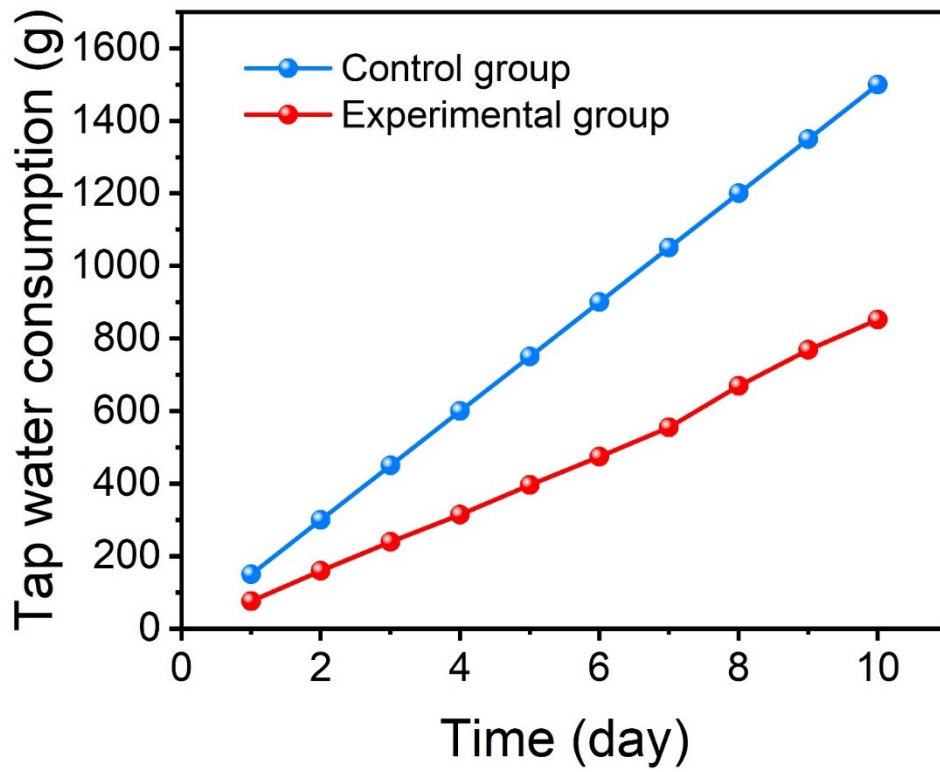


Fig. S21 Comparison of tap water consumption between the control group and the experimental group.

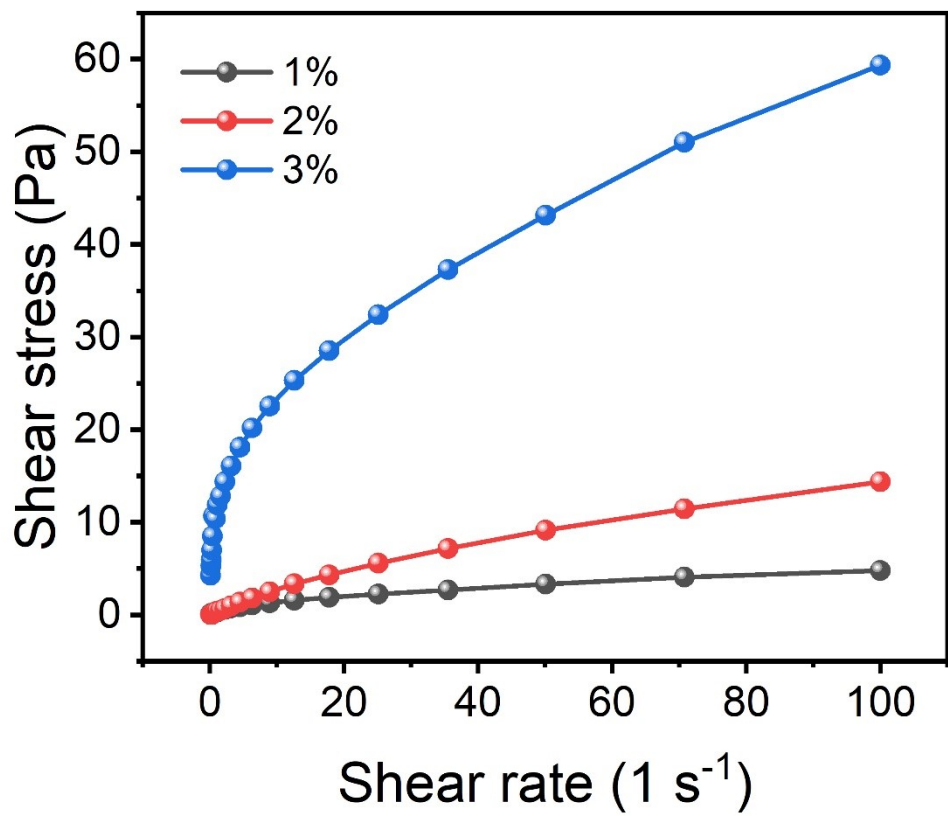


Fig. S22 Relationship curve between shear rate and shear stress of PEO at different concentrations.

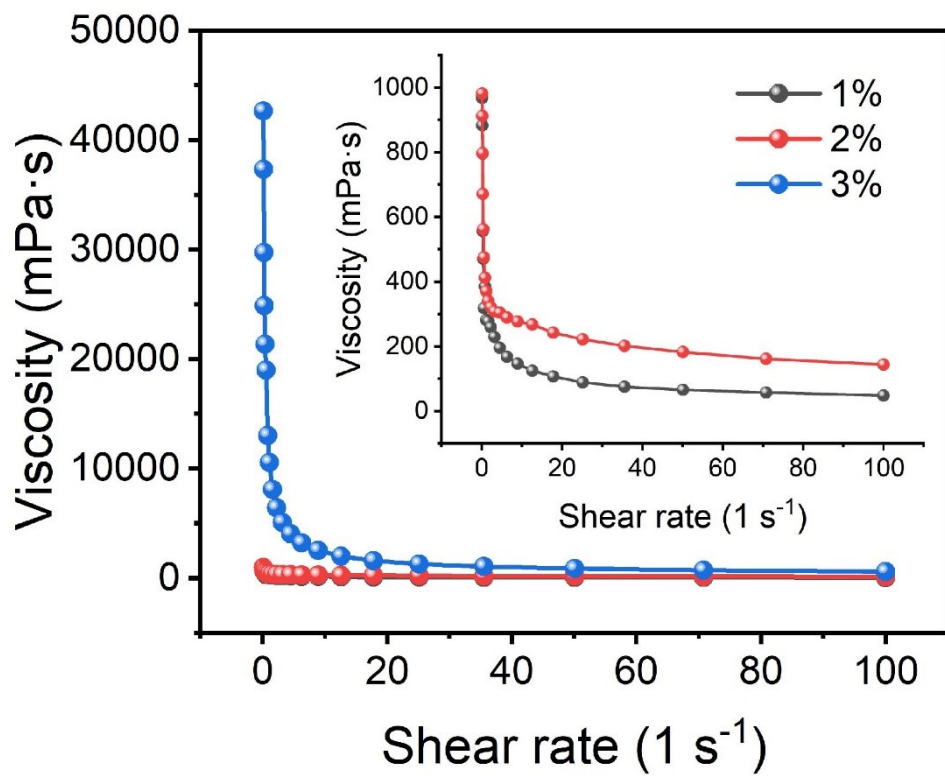


Fig. S23 Viscosity curves of PEO at different concentrations.

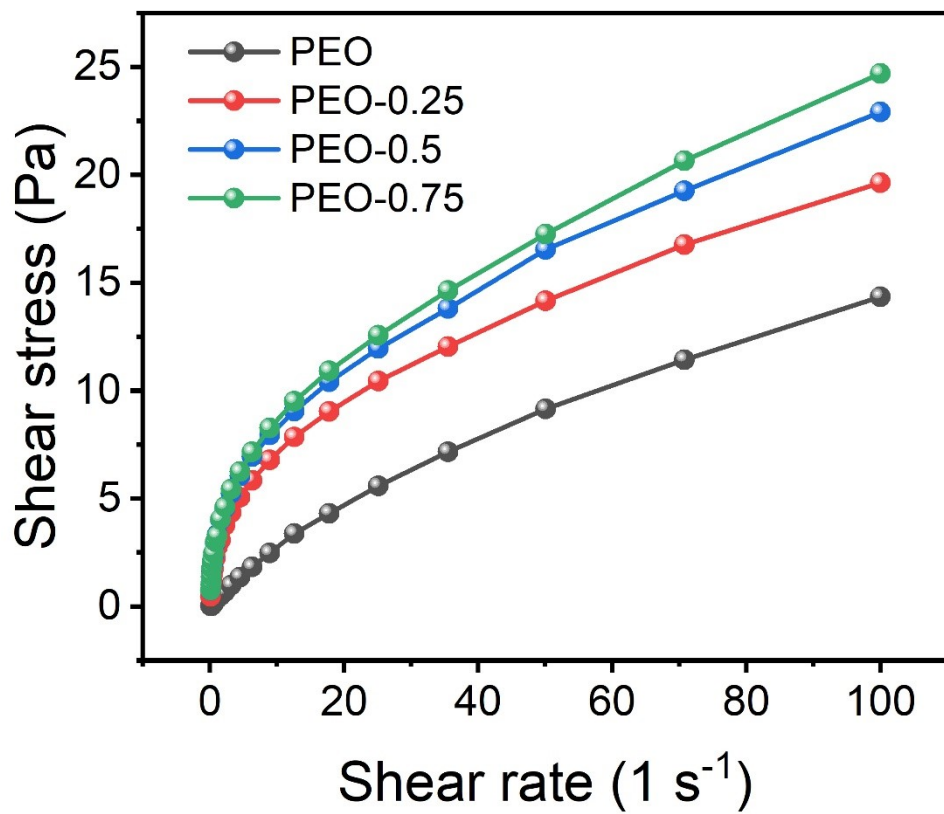


Fig. S24 Relationship curve between shear rate and shear stress of different samples.

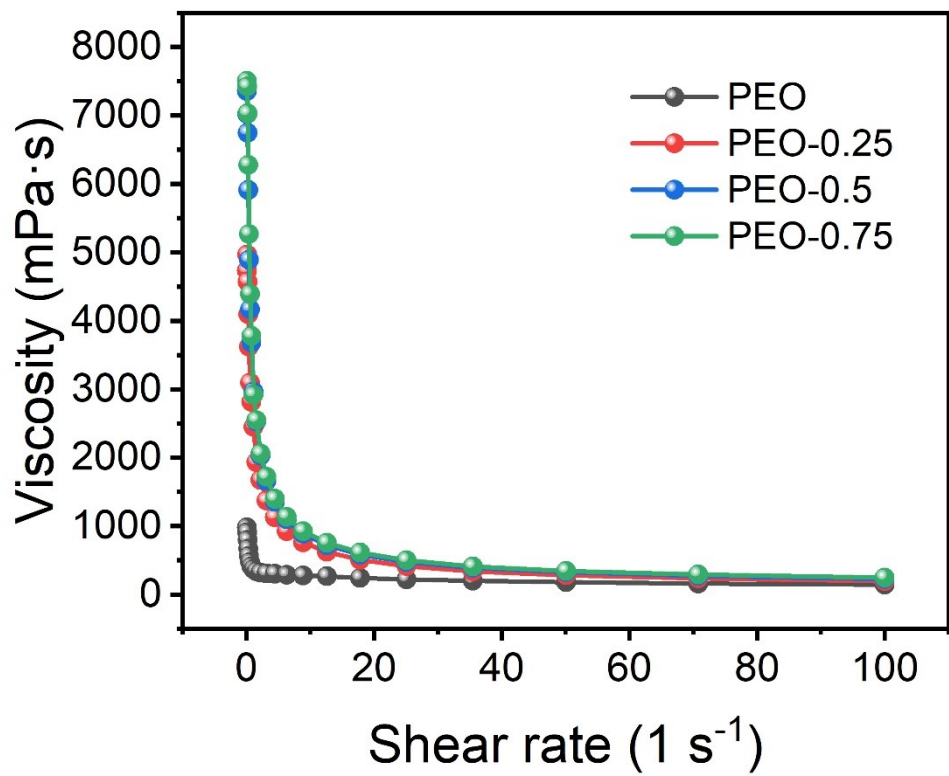


Fig. S25 Viscosity curves of different samples.

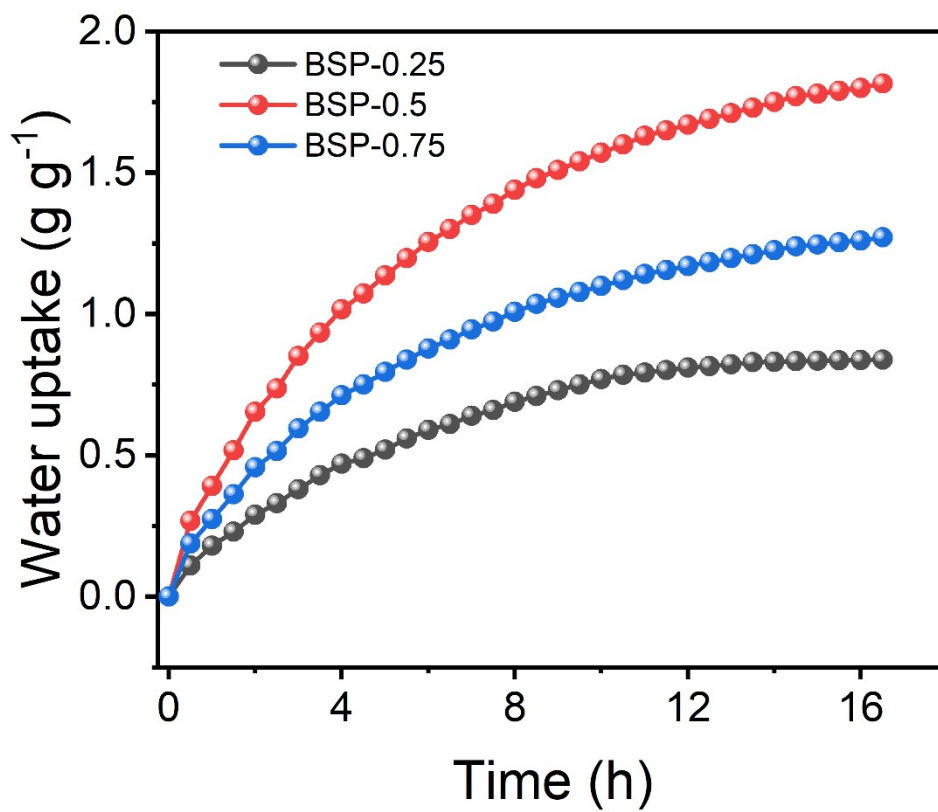


Fig. S26 Hygroscopicity of samples with different lithium chloride concentrations.

Table S1 Comparison of atmospheric water harvesting performance of various materials.

Materials	Adsorption Capacity [g g ⁻¹]	Desorption temperature	References
MOF-801	0.25 (20% RH, 25 °C)	1 sun (66°C)	[1]
MOF-303	0.21 (20% RH, 25 °C)	1 sun (70 °C)	[2]
MIL-101	1.01 ($p/p_0=5.6$ kPa, 40 °C)	140 °C	[3]
AlPO ₄ -LTA	0.42 ($0.10 < p/p_0 < 0.15$)	75 °C	[4]
LiCl@CGNFC	1.23 (90% RH, 25 °C)	1 sun (28.8-130.1 kLx)	[5]
N-MAG	0.72 (35.2-56.8% RH, 23.1-29.0 °C)	60 °C	[6]
HMGs	0.5-0.8 (15-30% RH, 25 °C)	60 °C	[7]
LiCl/PMS/CNTs	1.26-1.81 (15-30% RH, 25 °C)	1 sun (75 °C)	[8]
SHPFs	0.64-0.96 (15-30% RH, 25 °C)	60 °C	[9]
SPHN	0.78-2.01 (30-80% RH, 25 °C)	0.7-1.0 kWm ⁻² solar irradiation	[10]
Li-SHC	1.18 (15% RH, 15 °C)	110 °C	[11]
PPy-COF@Trilayer-LiCl	0.77-2.56 (30-80% RH, 25 °C)	1 sun (75.3 °C)	[12]
LiCl@rGO-SA	1.52 (30% RH, 30 °C)	90 °C	[13]
Ultra-sponge	1.82 (70% RH, 25 °C)	1 sun (450 W/m ²)	This work

Table S2 Comparison of stable cyclic performance of various materials at 60% RH.

Materials	Cycle times	Adsorption capacity [g g ⁻¹] /60% RH	References
LiCl/PMS/CNTs	35	3.13	[8]
ZHPC-3 hydrogel	10	1.67	[14]
PCP@LiCl	6	1.48	[15]
MTB- LiCl	100	0.75	[16]
HIPG	30	2.03	[17]
San-PAN	10	2.68	[18]
SA/CNTs/MC	100	0.77	[19]
CNF/LiCl-1.5	10	1.30	[20]
TCP-Li	15	2.50	[21]
SM@LiCl	16	2.20	[22]
ACFF	25	0.47	[23]
Cu ₃ (HHTP) ₂	14	0.28	[24]
Ultra-sponge	100	1.69	This work

Table S3 Comparison of actual production performance of various materials.

Materials	Cost [yuan/g]	Scalability	References
MOF-801	7.2	+	[1]
N-MAG	6.3	+++	[6]
PPy- COF@Trilayer- LiCl	4.4	++	[12]
LiCl@rGO-SA	3.7	++	[13]
Ultra-sponge	0.9	+++	This work

+: Difficult, ++: Medium, +++: Easy

References

- [1] Kim, H. et al. Water harvesting from air with metal-organic frameworks powered by natural sunlight. *Science* 356, 430-434 (2017).
- [2] Song, W. et al. MOF water harvester produces water from Death Valley desert air in ambient sunlight. *Nat. Water* 1, 626-634 (2023).
- [3] Ehrenmann, J. et al. Water adsorption characteristics of MIL-101 for heat transformation applications of MOFs. *Eur. J. Inorg. Chem.* 2011, 471-474 (2011).
- [4] Krajnc, A. et al. Superior performance of microporous aluminophosphate with LTA topology in solar-energy storage and heat reallocation. *Adv. Energy Mater.* 7, 1601815 (2017).
- [5] Chen, B. et al. All-natural, eco-friendly composite foam for highly efficient atmospheric water harvesting. *Nano Energy* 110, 108371 (2023).
- [6] Dai, M. et al. A nanostructured moisture-absorbing gel for fast and large-scale passive dehumidification. *Adv. Mater.* 34, 2200865 (2022).
- [7] Guan, W. et al. Hygroscopic-microgels-enabled rapid water extraction from arid air. *Adv. Mater.* 36, 2207786 (2022).
- [8] Guo, H. et al. Super moisture-sorbent sponge for sustainable atmospheric water harvesting and power generation. *Adv. Mater.* 36, 2414285 (2024).
- [9] Guo, Y. et al. Scalable super hygroscopic polymer films for sustainable moisture harvesting in arid environments. *Nat. Commun.* 13, 2671 (2022).

- [10] Han, X. et al. Efficient atmospheric water harvesting of superhydrophilic photothermic nanocapsule. *Small* 19, 2303358 (2023).
- [11] Shan, H. et al. Exceptional water production yield enabled by batch-processed portable water harvester in semi-arid climate. *Nat. Commun.* 13, 5406 (2022).
- [12] Xia, M. et al. Biomimetic hygroscopic fibrous membrane with hierarchically porous structure for rapid atmospheric water harvesting. *Adv. Funct. Mater.* 33, 2214813 (2023).
- [13] Xu, J. et al. Ultrahigh solar-driven atmospheric water production enabled by scalable rapid-cycling water harvester with vertically aligned nanocomposite sorbent. *Energy Environ. Sci.* 14, 5979-5994 (2021).
- [14] Guan, W. et al. Molecularly functionalized biomass hydrogels for sustainable atmospheric water harvesting. *Adv. Mater.* 37, 2420319 (2025).
- [15] Wang, J. et al. Tillandsia-inspired ultra-efficient thermo-responsive hygroscopic nanofibers for solar-driven atmospheric water harvesting. *Adv. Mater.* 37, 2408977 (2025).
- [16] Yang, K. et al. A solar-driven atmospheric water extractor for off-grid freshwater generation and irrigation. *Nat. Commun.* 15, 6260 (2024).
- [17] Yang, X. et al. Enhanced continuous atmospheric water harvesting with scalable hygroscopic gel driven by natural sunlight and wind. *Nat. Commun.* 15, 7678 (2024).
- [18] Yu, Z. et al. Phospholipid bilayer inspired sandwich structural nanofibrous membrane for atmospheric water harvesting and selective release. *Nano Lett.* 24, 2629-2636 (2024).
- [19] Zhang, X. et al. Autonomous atmospheric water harvesting over a wide RH range enabled by super hygroscopic composite aerogels. *Adv. Mater.* 36, 2310219 (2024).
- [20] Zhu, P. et al. 3D printed cellulose nanofiber aerogel scaffold with hierarchical porous structures for fast solar-driven atmospheric water harvesting. *Adv. Mater.* 36, 2306653 (2024).
- [21] Zou, H. et al. Solar-driven scalable hygroscopic gel for recycling water from passive plant transpiration and soil evaporation. *Nat. Water* 2, 663–673 (2024).
- [22] Chen, J. et al. A super-hygroscopic SA-MXene@LiCl composite membrane with fast ab/desorption kinetics for efficient sorption-based atmospheric water harvesting. *Desalination* 595, 118319 (2025).
- [23] Li, Y. et al. Rapid in-situ electric swing adsorption and efficient semiconductor refrigeration coupling for scaled-up sorption-based atmospheric water harvesting. *Energy Convers. Manage.* 326, 119469 (2025)
- [24] Wei, Y. et al. Free-standing MOF film with hierarchical porous structure for efficient solar-powered atmospheric water harvesting. *Chem. Eng. J.* 503, 158426 (2025).